AGU PUBLICATIONS

Geochemistry, Geophysics, Geosystems

RESEARCH ARTICLE
10.1002/2014GC005314

Isotope and trace element insights into heterogeneity of subridge mantle

Soumen Mallick[1,3], Henry J. B. Dick[2], Afi Sachi-Kocher[1], and Vincent J. M. Salters[1]

[1]National High Magnetic Field Laboratory, Department of Earth, Ocean and Atmospheric Science, Florida State University, Tallahassee, Florida, USA, [2]Woods Hole Oceanographic Institution, Department of Marine Geology and Geophysics, Woods Hole, Massachusetts, USA, [3]Department of Geological Sciences, Brown University, Providence, Rhode Island, USA

Key Points:
- The subridge mantle can have several lithologies with different solidii
- The melts that have impregnated some abyssal peridotites are aggregated melts
- The subridge mantle is relatively young in age

Supporting Information:
- ReadMe
- Tables S1-S4
- Photos 1-5
- Analytical Techniques

Correspondence to:
V. J. M. Salters,
salters@magnet.fsu.edu

Citation:
Mallick, S., H. J. B. Dick, A. Sachi-Kocher, and V. J. M. Salters (2014), Isotope and trace element insights into heterogeneity of subridge mantle, *Geochem. Geophys. Geosyst.*, *15*, 2438–2453, doi:10.1002/2014GC005314.

Received 27 FEB 2014
Accepted 22 MAY 2014
Accepted article online 28 MAY 2014
Published online 16 JUN 2014

This article was corrected on 9 JULY 2014. See the end of the full text for details.

Abstract Geochemical data for abyssal peridotites are used to determine the relationship to mid-ocean ridge basalts from several locations at ridge segments on the SW Indian Ridge (SWIR), the Mid-Cayman-Rise (MCR), and the Mid-Atlantic Ridge (MAR). Based on chemical and petrological criteria peridotites are categorized as being either dominantly impregnated with melt or being residual after recent melting. Those that are considered impregnated with melt also have isotopic compositions similar to the basalts indicating impregnation by an aggregate MORB melt. A SWIR and MCR residual peridotite Nd-isotopic compositions partly overlap the Nd-isotopic compositions of the basalts but extend to more radiogenic compositions. The differences between peridotite and basalt Nd-isotopic compositions can be explained by incorporating a low-solidus component with enriched isotopic signature in the subridge mantle: a component that is preferentially sampled by the basalts. At the MAR, peridotites and associated basalts have overlapping Nd-isotopic compositions, suggesting a more homogeneous MORB mantle. The combined chemistry and petrography indicates a complex history with several depletion and enrichment events. The MCR data indicate that a low-solidus component can be a ubiquitous component of the asthenosphere. Residual abyssal peridotites from limited geographic areas also show significant chemical variations that could be associated with initial mantle heterogeneities related to events predating the ridge-melting event. Sm-Nd model ages for possible earlier depletion events suggest these could be as old as 2.4 Ga.

1. Introduction

Decompression melting of adiabatically upwelling mantle beneath the mid-ocean ridges produces basaltic melts and a residual mantle depleted in elements that preferentially enter the melt phase. The upper part of this residual mantle is sampled as abyssal peridotites [e.g., *Dick and Bullen*, 1984; *Dick et al*., 1984; *Michael and Bonatti*, 1985]. Therefore, the compositions of abyssal peridotites sampled from the mid-ocean ridges provide information on melt extraction processes, composition of the residual mantle, and allow inferences to be made about the initial source composition of the mantle. Abyssal peridotites range in composition from lherzolite to harzburgite. When sufficient data are collected to be representative of outcrop scale variations, their average modal and mineral compositions correlate well with regional basalt chemistry; peridotites with less modal diopside have more refractory mineral compositions and are spatially associated with more refractory Na-poor basalts [*Dick et al*., 1984]. Moreover, peridotites dredged from the vicinity of mantle hot spots show greater depletion in chemical composition and lower modal abundances of diopside, while those away from the hot spots are less depleted [*Dick et al*., 1984; *Johnson et al*., 1990; *Zhou and Dick*, 2013].

Snow et al. [1994] first reported Sr and Nd-isotopic compositions of diopside separate from abyssal peridotites from the Southwest Indian Ridge (SWIR). With the exception of one radiogenic Nd sample, all were within the range of the nearby ridge basalts. Subsequent studies of peridotites from the Garrett Fracture Zone at the East Pacific Rise (EPR) [*Wendt et al*., 1999] and from the Vema Fracture Zone at the Mid-Atlantic Ridge (MAR) [*Cipriani et al*., 2004] observed the same. In contrast, *Salters and Dick* [2002] reported Nd-isotopic compositions of abyssal peridotites from the SWIR that are on average more radiogenic than the spatially associated ridge basalts. *Warren et al*. [2009] also presented isotope data for the SWIR with peridotites with $^{143}Nd/^{144}Nd$ overlapping with spatially associated basalts as well as more radiogenic compositions, though they found global averages that were similar (0.513167 versus 0.513061). *Cipriani et al*. [2011] measured two peridotites from the SWIR with significantly more radiogenic Nd-isotopic composition than the associated basalts [*Meyzen et al*., 2005, 2007]. Recently, *Stracke and Snow* [2009] and *Stracke et al*. [2011]

reported Gakkel Ridge peridotite Nd and Hf isotope compositions that are more radiogenic than the associated basalts. To explain the differences in Nd-isotopic composition between abyssal peridotites and MORB. *Salters and Dick* [2002] proposed that a component with a lower solidus and low $^{143}Nd/^{144}Nd$ could preferentially contribute to MORB magmatism.

This study assesses the nature of subridge mantle heterogeneity by investigating major and trace element contents and Sr and Nd-isotope ratios of peridotite diopside separates from the Southwest Indian Ridge (16.64°E, 15.23°E, and 9.98°E), Mid-Cayman-Rise, and Mid-Atlantic-Ridge (Kane FZ and 22°S). These locations were chosen because ridge depth and basalt chemistry suggests relatively low degrees of melting at all three locations. If a low-solidus component is present in the mantle source then its relative contribution to the melt will be greater at lower degrees of melting. If this low-solidus component also has an enriched isotope signature then these low-degree melts are expected to have an isotopic contrast with the host peridotites. By choosing these three locations, we have biased our study toward observing isotopic differences between basalt and peridotite. Furthermore, the MAR and MCR ridge segments are far from any hot spot influence, while our SWIR samples are associated with basalts with a Bouvet hot spot isotope signature [*le Roex et al*., 1992; *Mahoney et al*., 1989]. The MCR and MAR locations are thus a test on whether a low-solidus component exists in a normal-type MORB source.

2. Geological Setting of the Study Areas and Sample Description

2.1. Southwest Indian Ridge

The SWIR is an ultraslow-spreading mid-ocean ridge with an average full-spreading rate of 14–15 mm/yr, extending ~7700 km from the Bouvet to the Rodrigues Triple Junction. Bouvet and Marion islands, two near-ridge hot spots, are associated with long ocean ridge rises cut by numerous large-offset transforms. The geochemical signatures of both hot spots extend over large sections of the SWIR [*le Roex et al*., 1989, 1992; *Mahoney et al*., 1989; *Meyzen et al*., 2005]. Locally, highly oblique spreading reduces the rate of mantle upwelling, thickens the conductive lid, and limits mantle melting [*Dick et al*., 2003; *Montesi and Behn*, 2007; *Standish et al*., 2008]. In addition, a previously depleted initial mantle source composition beneath much of the SWIR can explain the limited crust production over large parts of this ridge [*Zhou and Dick*, 2013]. Dredge locations are on two super segments, bounded by the Du Toit Fracture Zone in the east and by the Shaka Fracture Zone in the west, representing areas where crust production ranges from moderate to very low. This region is devoid of transform faults, consisting of the western 9°E–16°E oblique spreading super segment and the eastern 16°E–25°E orthogonal spreading super segment. The 9°E–16°E super segment has an obliquity of up to ~57° from the spreading direction, and consists of linked oblique amagmatic rifts and widely spaced short orthogonal magmatic segments. The seafloor away from the magmatic segments consists of mantle peridotite with only scattered basalt flows [*Dick et al*., 2003; *Grindlay et al*., 1991; *Standish et al*., 2008]. The 16°E–25°E ridge consists of short en echelon second-order magmatic ridge segments subperpendicular to the spreading direction separated by nontransform offsets [*Dick et al*., 2003; *Standish et al*., 2008].

Dredge VAN7–78 at 16.64°E recovered plagioclase-bearing peridotites from a small nontransform offset between two magmatic segments. We analyzed three harzburgites and two lherzolites from this dredge. Dredge VAN7–85 at ~15.23°E from the south wall of a ~70 km long oblique amagmatic segment recovered spinel peridotites. We analyzed five lherzolites and two harzburgites from this dredge. *Warren et al*. [2009] analyzed five peridotites from this dredge.

Dredge VAN7–96 was located at 9.98°E on the eastern inside-corner high of the 195 km offset Shaka FZ, which juxtaposes old-cold lithosphere on the west against a short amagmatic segment 11° oblique to the spreading direction. The dredge recovered lherzolites with atypically abundant websterite veins. We analyzed two spinel lherzolites and a plagioclase harzburgite, while *Warren et al*. [2009] also report REE concentrations and Nd-isotope and Sr-isotope for nine additional samples, including olivine and plagioclase-bearing websterite veins.

Basalts from the SWIR show large variations in major and trace element and isotopic composition [*le Roex et al*., 1983, 1989, 1992; *Mahoney et al*., 1992, 1989; *Standish et al*., 2008]. Mid-ocean ridge basalts from 9°E to 25°E include N-MORB and E-MORB as well as nepheline-normative alkali basalts. These are interpreted as low-degree melts (3–5%) reflecting a variably veined and metasomatized mantle source previously enriched

by the Bouvet plume [*le Roex et al*., 1992; *Standish et al*., 2008], which was near this portion of the ridge approximately 20 Ma ago [*Georgen and Lin*, 2003].

2.2. Mid-Cayman Rise

The MCR is a 110 km long ultraslow spreading ridge with a half-spreading rate of 10 mm/yr [*Macdonald and Holcombe*, 1978]. Like the SWIR 9°E–16°E segment, the MCR rift valley floor is 1–2 km deeper than most slow spreading ridge segments [~3 km, *White et al*., 2001]. The rift valley is bounded by steep fault scarps exposing a variety of rocks including gabbro and peridotite [*Thompson et al*., 1980]. We analyzed 11 harzburgites and lherzolites including seven with plagioclase. Ten samples are from two dredges on the eastern wall of the rift valley near the segment center [*Dick et al*., 1984], and one is from an Alvin dive near the southern ridge-transform intersection (Table 1).

MCR basalts have a limited range of major element composition with high Na_2O ($Na_{8.0} \sim 3.8$) and TiO_2 (up to 2.5 wt %) compared to typical MORB [*Elthon*, 1992; *Perfit*, 1976; *Perfit and Heezen*, 1978; *Thompson et al*., 1980]. The high Na_2O and TiO_2 contents and the large ridge depth indicate low-degree mantle melting [*Dick et al*., 1984; *Klein and Langmuir*, 1987; *Thompson et al*., 1980]. The majority of the basalts are transitional MORB based on the K_2O/TiO_2 ratio and have $(La/Sm)_N < 1$ and $(La/Yb)_N > 1$ (N stands for chondrite-normalized). We analyzed 27 basalts (see supporting information Table S2), mostly from the segment center and near the northern ridge-transform intersection for major and trace element and isotopic composition.

2.3. Mid-Atlantic Ridge

Our samples include eight peridotites, one plagioclase-bearing, from Dredge AII-96-1 on the southern Kane Transform wall 170 km west of the MARK area of the Mid-Atlantic Ridge on ~11–12 Ma crust, and two peridotites from Dredge AII-60-9 at the ~22°S Fracture Zone (Tables 1 and 2). The midpoint of the MAR axis at 23°N is ~3600 m deep lying close to the southern end of the Azores Rise over 2200 km from the Azores hot spot. The majority of the basalts from MARK are N-MORBs, but a few E-MORBs exist [*Bryan et al*., 1981; *Donnelly et al*., 2004; *Reynolds and Langmuir*, 1997]. MARK area basalts have moderately high Na_2O [$Na_{8.0} \sim$ 2.67–2.93; *Reynolds and Langmuir*, 1997] indicating low degrees of mantle melting, consistent with geologic evidence for thin crust [*Dick et al*., 2008, 2010]. The Nd-isotopic composition of the MARK basalts shows significant variability [0.513139–0.513365, *Donnelly et al*., 2004; *Ito et al*., 1987; *Salters*, 1996] and extend to the most radiogenic Nd and unradiogenic Sr-isotopic compositions of the ocean basins. Basalts from the 22°S Fracture Zone are typical normal MORBs with $^{87}Sr/^{86}Sr = 0.7022–0.7028$ and $^{143}Nd/^{144}Nd \sim 0.5131$ [*Ito et al*., 1987].

3. Results

Analytical methods are described in the supporting information. Major element compositions of diopside and spinel in abyssal peridotites are listed in Table 1, and are illustrated in Figure 1. Trace element concentrations and isotopic compositions of diopside are listed in Table 2. Isotope analyses were done on diopside separates as they contain the bulk of the peridotite REE content and are more resistant to alteration than the other silicates. Although a reliable Nd-isotope composition can be extracted, alteration is so extensive that the Sr-isotopic composition is often exchanged with seawater and must be considered a maximum value. All Sr-isotope compositions are, however, much lower than seawater values. Based on the Sr/Nd ratios in the peridotite and in seawater the Nd-isotopes of the peridotites are not altered by seawater.

Short petrographic descriptions are given in supporting information Table S1. Our samples are all mantle tectonites with fabrics ranging from protogranular to mylonitic, reflecting varying stages of deformation from the earliest mantle flow fabric to late-stage high-temperature and brittle deformation associated with the formation of detachment and block faults that unroofed the peridotites (see photo 1 in Table S1). Their original mineralogy consists largely of olivine, subordinate enstatite, and lesser amounts of diopside (see photos 2 and 3 in Table S1 as common occurrence of enstatite and diopside). Chromium spinel, usually fresh, is a ubiquitous accessory mineral, though in some cases it is altered to ferritchromite. Plagioclase is, or was present in many samples; generally entirely, or more rarely partially, pseudomorphed by prehnite, chlorite, or hydrogrossular (see photo 4 in Table S1). Fresh relict plagioclase, however, is rare. Alteration generally followed crystal-plastic deformation, with extensive static replacement of pyroxene and olivine by serpentine, followed by late seafloor weathering of relict olivine to clay. In a few cases, pyroxene is heavily

AGU Geochemistry, Geophysics, Geosystems

10.1002/2014GC005314

Table 1. Average Clinopyroxene and Spinel Major Element Compositions of Abyssal Peridotites (wt %)

	Latitude	Longitude	Lithology	Residual or Impregnated		SiO_2	TiO_2	Al_2O_3	Cr_2O_3	MnO	MgO	FeO	CaO	Na_2O	K_2O	Total	Mg#	Cr#
Southwest Indian Ridge																		
VAN7–78-36H	52.38°S	16.64°E	Plagioclase Harzburgite	Impregnated	cpx(5)[a]	53.93(51)	0.29(5)	2.04(30)	0.70(16)	0.08(6)	16.92(37)	2.23(15)	24.18 (62)	0.26 (4)		100.62	0.93	0.19
					spl(10)	0.02(3)	0.38(3)	26.25(52)	38.20(82)	0.27(7)	12.53(45)	22.17(30)	0.01(1)	0.01(1)	0.00	99.09	0.51	0.49
VAN7–78-36V	52.38°S	16.64°E	Plagioclase Harzburgite	Impregnated	cpx(6)	53.44(41)	0.53(6)	2.52(32)	0.92(15)	0.11(4)	16.23(29)	2.27(8)	23.63(56)	0.41(1)	0.01(1)	100.08	0.93	0.20
VAN7–78-37H	52.38°S	16.64°E	Plagioclase Harzburgite	Impregnated	cpx(6)	51.77(105)	0.23(4)	4.79(163)	1.06(4)	0.08(6)	15.35(60)	2.91(29)	23.44(50)	0.40(4)		100.02	0.90	0.13
					spl(10)	0.00	0.30(3)	26.58(29)	35.76(44)	0.24(4)	12.07(16)	23.74(69)	0.00	0.01(1)	0.00	98.69	0.48	0.47
VAN7–78-39	52.38°S	16.64°E	Plagioclase Lherzolite	Impregnated	cpx(6)	52.54(92)	0.28(4)	3.07(137)	1.09(27)	0.08(5)	16.00(41)	2.53(23)	23.10(24)	0.48(1)	0.01(2)	99.17	0.92	0.19
					spl(10)	0.02(1)	0.46(3)	22.46(29)	38.71(72)	0.38(9)	10.89(13)	25.59(52)	0.0191)	0.01(1)	0.00	98.53	0.43	0.53
VAN7–78-41	52.38°S	16.64°E	Plagioclase Lherzolite	Impregnated	cpx(5)	52.87(14)	0.22(5)	4.22(209)	1.08(20)	0.13(7)	15.45(142)	2.62(25)	23.09(100)	0.33(7)	0.01(1)	100.04	0.91	0.15
					spl(10)	0.01(10	0.33(30	23.28(67)	38.71(134)	0.26(6)	12.06(82)	24.53(142)	0.00	0.01(1)	0.00	99.19	0.47	0.53
VAN7–85-30	52.25°S	15.23°E	Spinel Lherzolite	Residual	cpx(9)	51.41(47)	0.20(2)	6.65(24)	1.08(3)	0.11(27)	15.83(92)	2.87(9)	21.62(62)	0.38(1)	0.01(10)	100.15	0.91	0.10
					spl(10)	0.00	0.06(2)	48.52(1.26)	17.25(195)	0.12(6)	18.21(29)	13.13(63)	0.01(1)	0.01(1)	0.00	97.31	0.71	0.19
VAN7–85-33	52.25°S	15.23°E	Spinel Harzburgite	Residual	cpx(5)	51.37(29)	0.19(3)	6.87(15)	0.99(10)	0.07(5)	16.34(125)	3.10(50)	21.12(158)	0.37(8)	0.01(1)	100.43	0.90	0.09
					spl(10)	0.00	0.06(2)	48.38(120)	16.78(116)	0.11(4)	18.18(99)	13.65(148)	0.01(1)	0.03(4)	0.01(3)	97.21	0.70	0.19
VAN7–85-37	52.25°S	15.23°E	Meta-Peridotite		spl(10)	0.00	0.31(3)	24.41(37)	38.66(51)	0.22(7)	11.76(14)	25.08(33)	0.00	0.01(1)	0.00	100.46	0.46	0.51
VAN7–85-42	52.25°S	15.23°E	Spinel Lherzolite	Residual	cpx(7)	51.21(48)	0.21(2)	6.79(13)	1.03(12)	0.10(4)	15.85(172)	2.93(39)	22.00(227)	0.39(5)		100.51	0.91	0.09
					spl(10)	0.00	0.06(2)	47.95(47)	17.51(57)	0.12(7)	19.01(13)	12.85(32)	0.01(1)	0.01(1)	0.01(1)	97.52	0.73	0.20
VAN7–85-43	52.25°S	15.23°E	Spinel Lherzolite	Residual	cpx(9)	51.79(67)	0.17(3)	6.33(35)	1.13(16)	0.11(6)	16.68(85)	2.97(38)	21.03(118)	0.40(6)		100.61	0.91	0.11
					spl(10)	0.00	0.05(2)	46.80(34)	17.33(89)	0.16(7)	18.03(31)	14.97(31)	0.00	0.02(1)	0.00	97.36	0.68	0.20
VAN7–85-44	52.25°S	15.23°E	Spinel Lherzolite	Residual	cpx(10)	51.89(60)	0.24(2)	6.12(26)	1.18(11)	0.12(4)	16.33(89)	2.76(23)	21.43(108)	0.52(8)		100.59	0.91	0.11
					spl(10)	0.00	0.11(2)	44.11(49)	21.99(52)	0.16(6)	18.55(20)	13.18(26)	0.01(1)	0.01(1)	0.00	98.11	0.72	0.25
VAN7–85-47	52.25°S	15.23°E	Spinel Lherzolite	Residual	cpx(4)	50.59(69)	0.20(2)	6.62(26)	1.09(12)	0.12(12)	15.87(77)	2.91(15)	21.50(88)	0.37(1)		99.27	0.91	0.10
					spl(10)	0.01(1)	0.05(2)	48.17(33)	17.12(310	0.12(5)	18.82(21)	12.96(19)	0.01(1)	0.01(1)	0.01(1)	97.27	0.72	0.19
VAN7–96-28	53.14°S	9.98°E	Spinel Lherzolite	Impregnated	cpx(7)	51.72(31)	0.36(3)	7.31(4)	1.27(6)	0.09(4)	14.22(43)	2.78(19)	21.06(49)	1.45(1)	0.01(1)	100.27	0.90	0.10
					spl(10)	0.00	0.12(2)	47.96(34)	16.27(40)	0.13(5)	18.44(24)	13.93(21)	0.01(1)	0.07(13)	0.01(1)	96.94	0.70	0.18
VAN7–96-29	53.14°S	9.98°E	Spinel Lherzolite	Impregnated	cpx(7)	51.63(30)	0.38 (2)	7.18(20)	1.26(12)	0.08(4)	14.68 (60)	2.93(10)	20.53(97)	1.40(8)		100.07	0.90	0.11
					spl(10)	0.00	0.11(2)	47.44(24)	18.20(62)	0.18(4)	18.18(70)	14.72(56)	0.01(1)	0.01(1)	0.00	97.80	0.70	0.20
VAN7–96-31	53.14°S	9.98°E	Plagioclase Harzburgite	Impregnated	cpx(5)	52.33(60)	0.33(2)	6.19(11)	1.74(13)	0.10(5)	14.92(90)	2.47(16)	20.55(59)	1.57(28)		100.20	0.92	0.16
					spl(10)	0.00	0.17(2)	37.06(28)	29.11(52)	0.18(7)	15.93(14)	16.57(34)	0.00	0.02(1)	0.01(1)	99.04	0.63	0.34
Mid-Cayman Rise																		
OCE23-13-2	18.17°N	81.61°W	Spinel Harzburgite	Residual	cpx(7)	51.63(50)	0.20(3)	5.86(84)	0.95(20)	0.12(7)	15.46(43)	2.42(18)	23.79(44)	0.20(3)		100.64	0.92	0.10
					spl(10)	0.00	0.05(3)	50.05(25)	16.79(63)	0.12(5)	18.65(14)	11.49(38)	0.00	0.01(1)	0.00	97.16	0.74	0.18
OCE23-13-8	18.17°N	81.61°W	Spinel Harzburgite	Residual	cpx(7)	51.41(55)	0.21(3)	5.69(87)	0.93(19)	0.12(9)	15.64(47)	2.36(17)	23.20(32)	0.24(3)	0.01(1)	99.80	0.92	0.10
					spl(8)	0.00	0.06(2)	48.03(38)	19.12(64)	0.13(5)	18.43(14)	11.95(27)	0.01(1)	0.02(1)	0.00	97.75	0.73	0.21
OCE23-13-10	18.17°N	81.61°W	Plagioclase Harzburgite	Residual	cpx(5)	51.61(0.15)	0.19(2)	5.97(13)	1.08(9)	0.14(8)	15.95(87)	2.73(33)	22.30(98)	0.44(16)	0.01(1)	100.43	0.91	0.11
					spl(10)	0.00	0.09(1)	46.41(42)	21.07(96)	0.12(4)	18.36(13)	11.69(24)	0.00	0.01(1)	0.01(1)	97.77	0.74	0.23
OCE23-13-11	18.17°N	81.61°W	Spinel Lherzolite	Residual	cpx(6)	51.39(41)	0.17(2)	5.85(32)	1.14(5)	0.13(3)	15.56(14)	2.43(13)	23.65(30)	0.24(8)	0.01(1)	100.57	0.92	0.12
					spl(10)	0.00	0.07(2)	49.23(32)	19.18(41)	0.14(4)	18.13(21)	11.61(28)	0.00	0.01(1)	0.00	98.37	0.74	0.21
OCE23-13-50	18.17°N	81.61°W	Spinel Lherzolite	Residual	cpx(5)	51.29(34)	0.19(2)	6.16(8)	0.96(2)	0.10(20)	15.00(51)	2.43(6)	23.58(3)	0.24(1)	0.01(9)	99.95	0.92	0.09
					spl(10)	0.00	0.08(3)	47.53(31)	19.74(41)	0.12(8)	18.43(15)	11.56(25)	0.01(1)	0.01(1)	0.00	97.49	0.74	0.22
OCE23-14-1	18.21°N	81.54°W	Plagioclase Harzburgite	Residual	cpx(6)	51.66(29)	0.20(1)	5.82(30)	0.96(15)	0.05(4)	15.41(24)	2.35(19)	23.50(40)	0.30(2)		99.12	0.92	0.10
					spl(10)	0.00	0.06(1)	49.08(45)	17.80(53)	0.13(6)	18.18(18)	11.87(36)	0.01(1)	0.01(1)	0.00	97.14	0.73	0.19
OCE23-14-7	18.21°N	81.54°W	Plagioclase Harzburgite	Residual	cpx(8)	52.12(45)	0.25(22)	4.84(63)	1.06(8)	0.07(4)	16.17(46)	2.71(21)	23.43(79)	0.22(29)	0.01(1)	100.90	0.91	0.13
					spl(10)	0.00	0.22(3)	29.32(17)	36.32(79)	0.24(7)	13.93(14)	19.41(44)	0.00	0.01(1)	0.00	99.47	0.56	0.45
ALV616-1-1	17.38°N	81.69°W	Plagioclase Lherzolite	Impregnated	cpx(10)	51.66(41)	0.27(3)	6.17(470	1.12(13)	0.09(65)	15.59(131)	2.49(6)	22.00 983)	0.50(1)		100.56	0.92	0.11
					spl(10)	0.00	0.28(2)	30.78(58)	37.27(84)	0.21(6)	13.98(17)	17.19(57)	0.00	0.01(1)	0.00	99.72	0.59	0.45
OCE23-14-2	18.21°N	81.54°W	Plagioclase Harzburgite	Impregnated	cpx(4)	52.18(36)	0.18(2)	5.26(30)	1.14(8)	0.12(3)	15.50(15)	2.61(15)	22.78 (28)	0.31(5)		100.07	0.91	0.13
OCE23-14-3	18.21°N	81.54°W	Plagioclase Harzburgite	Impregnated	cpx(11)	52.09(74)	0.19(6)	5.24(60)	1.10(24)	0.10(97)	15.42(78)	3.02(6)	22.37(46)	0.63(1)	0.02(8)	100.18	0.90	0.12
OCE23-14-10	18.21°N	81.54°W	Plagioclase Harzburgite	Impregnated	cpx(8)	52.78(56)	0.22(2)	3.64(24)	1.21(4)	0.09(51)	16.03(40)	2.84(4)	22.78(50)	0.50(1)	0.01(17)	100.09	0.91	0.18
					spl(10)	0.00	0.43(3)	23.47(31)	41.17(42)	0.28(10)	11.40(21)	23.37(48)	0.00	0.01(1)	0.00	100.15	0.47	0.54

Table 1. (continued)

	Latitude	Longitude	Lithology	Residual or Impregnated		SiO_2	TiO_2	Al_2O_3	Cr_2O_3	MnO	MgO	FeO	CaO	Na_2O	K_2O	Total	Mg#	Cr#
Mid-Atlantic Ridge																		
All-96-1-3	23.81°N	46.57°W	Spinel Harzburgite	Residual	cpx(7)	51.43(50)	0.10(2)	5.15(19)	1.28(12)	0.12(6)	16.65(84)	2.93 (27)	21.71(88)	0.09(1)	0.01(1)	99.47	0.91	0.14
					spl(10)	0.00	0.08	37.54(20)	30.31(40)	0.17(7)	17.05(13)	14.08(25)	0.00	0.01(1)	0.00	99.25	0.68	0.35
All-96-1-7	23.81°N	46.57°W	Plagioclase Lherzolite	Residual	cpx(8)	51.49(54)	0.13(8)	5.53(270	1.24(12)	0.13(5)	16.80(44)	3.30(16)	20.78 (51)	0.27(7)	0.01(1)	99.66	0.90	0.13
					spl(10)	0.00	0.24(1)	35.51(47)	31.08(74)	0.21(7)	16.20(14)	16.08(29)	0.00	0.02(1)	0.00	99.35	0.64	0.37
All-96-1-19	23.81°N	46.57°W	Spinel Harzburgite	Residual	cpx(9)	51.38(74)	0.11(4)	5.74(25)	1.22(6)	0.08(8)	17.37(84)	3.38(24)	20.63(115)	0.06 (1)	0.01(1)	99.97	0.90	0.12
					spl(10)	0.00	0.04(3)	40.80(55)	26.32(43)	0.19(5)	16.71(19)	15.09(43)	0.00	0.01(1)	0.01(1)	99.18	0.66	0.30
All-96-1-24	23.81°N	46.57°W	Spinel Harzburgite	Residual	cpx(8)	52.04(29)	0.09(1)	4.87(22)	1.16(8)	0.10(4)	16.03(26)	2.88(18)	22.89 (46)	0.11(2)		100.17	0.91	0.14
					spl(10)	0.01(2)	0.07(2)	25.34(25)	43.28(80)	0.18(4)	14.23(16)	16.12(41)	0.01(1)	0.01(1)	0.01(1)	99.26	0.61	0.53
All-96-1-26	23.81°N	46.57°W	Spinel Harzburgite	Residual	spl(10)	0.00	0.08(2)	36.08(540	28.87(82)	0.20(9)	16.30(19)	15.53(40)	0.01(1)	0.01(10	0.00	97.09	0.65	0.35
All-96-1-31	23.81°N	46.57°W	Lherzolite	Residual	cpx(5)	50.64(72)	0.09(1)	5.76(34)	1.18(13)	0.10(5)	16.50(58)	3.44(9)	20.98(80)	0.09(6)		98.77	0.90	0.12
					spl(10)	0.01(2)	0.06(2)	39.30(24)	27.23(97)	0.14(5)	17.12(19)	13.35(36)	0.00	0.01(1)	0.01(1)	97.24	0.70	0.32
All-96-12-28HD5	23.52°N	43.91°W	Harzburgite	Residual	cpx(6)	52.25(113)	0.08(3)	4.61(40)	1.28(12)	0.11(4)	17.03(58)	2.77 (26)	21.24(83)	0.22(20)	0.01(1)	99.60	0.92	0.16
					spl(10)	0.00	0.05(2)	38.51(24)	28.06(38)	0.15(5)	16.99(20)	13.70(33)	0.00	0.01(1)	0.00	97.48	0.69	0.33
All-96-12-30	23.52°N	43.91°W	Spinel Harzburgite	Residual	cpx(6)	52.26(34)	0.09(2)	4.78(18)	1.29(6)	0.13(4)	16.80 (68)	2.80(24)	22.17(121)	0.09(2)		100.42	0.91	0.15
					spl(10)	0.01(2)	0.07(2)	33.89(21)	32.84(61)	0.22(4)	15.53(20)	14.96(42)	0.01(1)	0.01(1)	0.00	97.53	0.65	0.39
All-60-9-74	21.93°S	11.80°W	Spinel Harzburgite	Residual	cpx(10)	51.78(93)	0.10(3)	5.21(20)	1.30(14)	0.12(6)	16.05(61)	2.64 (25)	22.04(92)	0.38(6)		99.62	0.92	0.14
					spl(10)	0.00	0.06(2)	33.55(28)	33.89(161)	0.21(7)	15.40(28)	15.37(57)	0.01(1)		0.01(1)	98.50	0.64	0.40

[a]Number of spot analyzed.

altered to tremolitic amphibole (notably VAN7–85-37). Occasionally talc replaces enstatite (e.g., VAN7–85-44).

Plagioclase-bearing peridotites are generally associated with late-stage impregnation and reaction with transient MORB-like melts. Plagioclase in abyssal peridotites is often hard to recognize due its complete or nearly complete alteration. Petrographically, plagioclase is often localized near enstatite grains, typically interstitial to olivine and enstatite, and is often intergrown with vermiform spinel or interstitial late clinopyroxene [*Dick*, 1989]. In many examples plagioclase has a well-developed shape fabric, indicating a strong differential stress at the time of melt injection. A network of melt is shown by ALV616 1-1 (photo 5 in Table S1). Plagioclase trails (including plagioclase pseudomorphs) are also seen as being related to impregnation. Generally, where preserved, relic plagioclase is not recrystallized, suggesting that following injection of the melt, solid-state deformation mechanisms ceased.

Plagioclase can form due to exsolution from aluminous enstatite and diopside during reequilibration to lower pressures, though this typically occurs as blebs within the pyroxene. More typically, however, there is chemical evidence for impregnation provided by sodic plagioclase and high spinel $TiO_2 > 0.2$ wt % [e.g., *Dick and Bullen*, 1984]. Twenty of the peridotites, we have analyzed spinel TiO_2 content of 0.11 wt % or less, show no evidence of impregnation and are considered to be dominantly residual. Two peridotites: OCE23-14-7 from the MCR and All96-1-7 from the MAR are plagioclase peridotites with TiO_2 content above 0.2 wt %, while all other characteristics indicate a dominant residual character. All other peridotites from this study are considered impregnated to some degree.

3.1. Southwest Indian Ridge

Fifteen peridotites from three dredges were studied. The major element variations of the mineral phases overlap with previous work [*Warren et al.*, 2009]. The most depleted harzburgites and lherzolites with low TiO_2 spinel and diopside are restricted to one dredge VAN7–85. The molar Cr/(Cr + Al) ratios (Cr#) of the SWIR peridotite spinels span the entire range for abyssal spinel peridotites (see Figure 1). Two dredges from the SWIR (VAN7–78

Table 2. Trace Element Concentrations (μg/g) and Sr-Nd Isotope Ratios for Clinopyroxene From Abyssal Peridoties

	Ti	Zr	La	Ce	Nd	Sm	Eu	Gd	Tb	Dy	Er	Yb	Lu	$^{87}Sr/^{86}Sr$	2σ	$^{143}Nd/^{144}Nd$	2σ
Southwest Indian Ridge																	
VAN7–78-36H	2093	14.81	0.31	1.49	2.20	1.02	0.30	1.94	0.39	3.09	1.93	1.71	0.22	0.702858	±19	0.513044	±19
VAN7–78-36H	2978	26.81	0.55	2.74	3.65	1.60	0.48	2.54	0.45	3.33	1.97	1.68	0.22	0.702581	±352	0.513026	±12
VAN7–78-37H	1574	1.23	0.41	1.11	0.59	0.50	0.20	1.40	0.31	2.59	1.85	1.81	0.25	0.702915	±82	0.513003	±30
VAN7–78-39	1984	8.53	0.42	1.68	1.61	0.80	0.28	1.67	0.34	2.78	1.88	1.76	0.24	0.702992	±7	0.513031	±9
VAN7–78-41	1910	11.94	0.43	1.84	1.64	0.87	0.26	1.80	0.37	3.05	2.03	1.99	0.27	0.702800	±7	0.513046	±9
VAN7–85-30	1531	0.49	0.00	0.01	0.29	0.47	0.23	1.25	0.27	2.17	1.48	1.48	0.21	0.704899	±49	0.513321	±92
VAN7–85-33	1554	0.66	0.01	0.03	0.36	0.52	0.25	1.32	0.27	2.29	1.52	1.51	0.21	0.704583	±10	0.513173	±48
VAN7–85-37[a]														0.704460	±9	0.513086	±19
VAN7–85-42	1433	0.46	0.00	0.01	0.24	0.39	0.20	1.05	0.23	2.02	1.38	1.46	0.20	0.702440	±17	0.513319	±14
VAN7–85-43	1352	0.40	0.05	0.19	0.30	0.41	0.20	1.04	0.23	2.01	1.39	1.45	0.20	0.702902	±147	0.513320	±21
VAN7–85-44	1883	1.67	0.00	0.03	0.59	0.68	0.31	1.46	0.29	2.31	1.49	1.44	0.20	0.702762	±10	0.513269	±9
VAN7–85-47	1376	0.64	0.00	0.13	0.26	0.43	0.21	1.13	0.25	2.11	1.45	1.50	0.21	0.702308	±13	0.513323	±13
VAN7–96-28	3007	16.02	1.01	3.73	3.88	1.39	0.57	1.85	0.29	2.04	1.18	1.15	0.16	0.703032	±35	0.512933	±9
VAN7–96-29	2947	15.09	0.95	3.65	3.70	1.39	0.56	1.79	0.27	1.98	1.15	1.16	0.16	0.703041	±9	0.512921	±9
VAN7–96-31	2640	24.61	0.56	3.25	4.73	1.75	0.66	2.31	0.37	2.59	1.43	1.30	0.18	0.703239	±8	0.512885	±10
Mid-Cayman Rise																	
OCE23-13-2	1207	0.64	0.03	0.02	0.29	0.36	0.17	0.90	0.19	1.62	1.12	1.11	0.16	0.702608	±13	0.513256	±56
OCE23-13-8	1469	0.45	0.01	0.01	0.18	0.27	0.11	0.81	0.15	1.25	0.85	0.77	0.10	0.702942	±12	0.513199	±43
OCE23-13-10	1436	0.63	0.06	0.05	0.65	0.43	0.12	0.95	0.16	1.31	0.94	0.86	0.13	0.703043	±9	0.513141	±132
OCE23-13-11	1214	0.52	0.02	0.01	0.29	0.29	0.09	0.78	0.15	1.23	0.85	0.75	0.10	0.703756	±9		
OCE23-13-46														0.703371	±117	0.513111	±88
OCE23-13-50	1286	0.44	0.00	0.05	0.26	0.39	0.18	1.05	0.22	1.91	1.31	1.33	0.19	0.703721	±169	0.513278	±47
OCE23-14-1	1327	0.55	0.02	0.02	0.37	0.38	0.13	0.92	0.18	1.51	1.00	0.96	0.13	0.703238	±9	0.513154	±40
OCE23-14-2	1343	0.89	0.10	0.36	0.40	0.37	0.16	0.99	0.22	1.85	1.26	1.25	0.17	0.703350	±42	0.513122	±10
OCE23-14-3	1268	0.32	0.25	0.63	0.33	0.28	0.14	0.78	0.18	1.51	1.07	1.12	0.16	0.703194	±9	0.513139	±21
OCE23-14-4	3923	22.35	0.45	2.60	3.99	1.81	0.65	2.69	0.49	3.65	2.28	2.17	0.29	0.702569	±22	0.513120	±16
OCE23-14-7	1030	0.17	0.01	0.02	0.15	0.28	0.12	0.82	0.18	1.58	1.11	1.09	0.15	0.703317	±9	0.513131	±24
ALV616-1-1	1970	1.24	0.03	0.16	0.66	0.82	0.31	1.73	0.37	2.95	2.01	1.97	0.27	0.702552	±9	0.513425	±58
OCE23-14-10	1678	9.27	0.28	1.37	1.69	0.87	0.25	1.68	0.35	2.78	1.84	1.76	0.24	0.703039	±12	0.513139	±16
Mid-Atlantic Ridge																	
All-96-1-3	827	0.07	0.02	0.01	0.08	0.11	0.06	0.31	0.07	0.57	0.39	0.42	0.06	0.703468	±28	0.513148	±12
All-96-1-7	944	0.63	0.06	0.05	0.11	0.11	0.05	0.29	0.07	0.58	0.42	0.49	0.07	0.703083	±7	0.513163	±13
All-96-1-19	900	0.05	0.01	0.00	0.04	0.09	0.05	0.28	0.07	0.58	0.41	0.46	0.06			0.513011	±48
All-96-1-24	806	0.87	0.13	0.15	0.14	0.13	0.08	0.22	0.09	0.46	0.40	0.44	0.08			0.513171	±18
All-96-1-31	894	1.83	0.11	0.15	0.15	0.14	0.10	0.31	0.10	0.59	0.43	0.49	0.09			0.513190	±20
All-96-12-28 HD5	690	1.64	0.19	0.32	0.16	0.08	0.03	0.18	0.05	0.43	0.35	0.46	0.06	0.703711	±63	0.513165	±9
All-96-12-30	748	0.43	0.02	0.01	0.05	0.05	0.03	0.16	0.05	0.42	0.34	0.42	0.06	0.703884	±8	0.513156	±9
All-60-9-56																0.513135	±78
All-60-9-74	896	0.17	0.12	0.40	0.15	0.10	0.06	0.28	0.07	0.60	0.44	0.52	0.07	0.702759	±13	0.513144	±6

[a]Isotope ratios are measured in amphibole.

and VAN7–96) contain plagioclase lherzolites and harzburgites all with high TiO_2 spinels. One VAN7–78-36 peridotite contains a 2–3 mm wide gabbroic vein. SiO_2, Al_2O_3, and Mg# of the diopsides are relatively well correlated, and Na_2O and TiO_2 do not show correlations with other major elements.

REE patterns (Figure 2) for VAN7–78 show moderate LREE depletion with $(Ce/Yb)_N$ ranging from 0.16 to 0.43. We use Ce instead of La for the evaluation of the REE pattern as La shows sometimes, at low concentrations, a high La/Ce ratio that deviate from a smooth REE pattern. Of the REE pattern only La seems to be affected, and we attribute this to very late-stage (fluid) alteration which does not seem to affect Ce or the other REE. Diopside REE patterns for VAN7–96 are flat from Lu through Nd and have $(Ce/Yb)_N$ between 0.66 and 0.85 and Ce_N between 5.4 and 6.2. VAN7–96 samples have lower abundances of heavy REE (Yb_N varying from 7.14 to 8.06) than samples from the other dredges. Diopsides from VAN7–85 show large depletions in the light REE and a large compositional range: Ce_N ranges from 0.009 to 0.31 and $(Ce/Yb)_N$ ranges from 0.001 to 0.035. Heavy REE are relatively uniform with Yb_N varying from 8.93 to 9.39.

Nd-isotopic compositions are plotted in Figure 3 together with published data on peridotites and basalts. At mantle upwelling rates on the order of 10 mm/yr the postmelting radiogenic in-growth of the Nd-isotope affects the $^{143}Nd/^{144}Nd$ ratio at most at the tens of ppm level [$\ll$ 50 ppm; see also *Stracke et al.*, 2011; *Warren et al.*, 2009]. We thus consider that radiogenic in-growth after melting did not significantly affect the Nd-isotopic composition of the peridotites. Peridotites from VAN7–78 and VAN7–96 show a limited range in $^{143}Nd/^{144}Nd$: 0.513003–0.513046 and 0.512885–0.512933, respectively, which is within the range of $^{143}Nd/^{144}Nd$ of the associated basalts. In contrast, peridotites from dredge VAN7–85, with depleted

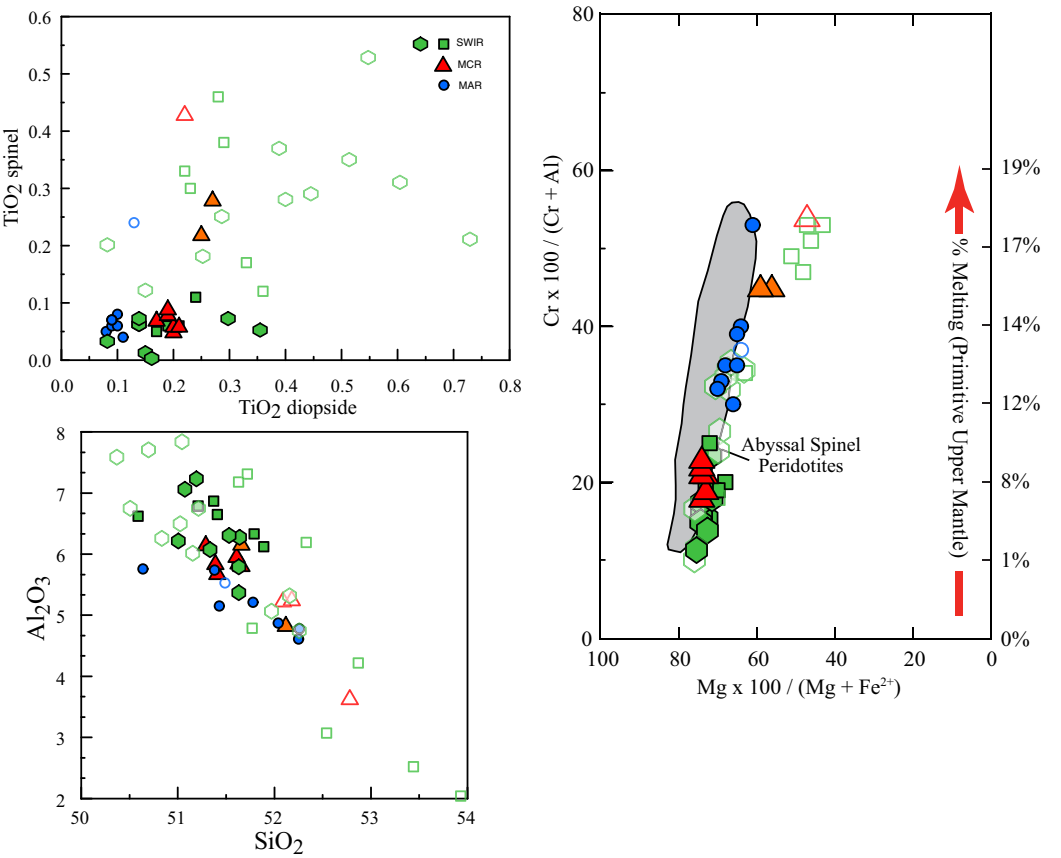

Figure 1. Major element variations of spinel and diopside in the studied peridotites. Symbols: green = SWIR, red = MCR, blue = MAR. Open symbols are for samples with spinels with >0.12 wt % TiO_2. Green hexagons are data from *Warren et al.* [2009].

REE patterns, display a large range in $^{143}Nd/^{144}Nd$ (0.513086–0.513323), which partially overlaps with the SWIR basalts and extend to more radiogenic compositions. *Warren et al.* [2009] showed similar results and they reported isotope data on three samples also analyzed in this study. The data from the two studies are within error of each other. The biggest difference is between analyses of sample VAN7–85-30, but both analyses have a relatively large error (0.019%).

3.2. Mid-Cayman Rise

Five MCR peridotites from dredge OCE23-13 show no petrographic evidence of melt impregnation. One of these harzburgites has metamorphic plagioclase; all have low TiO_2 spinels (<0.1 wt %, Figure 1) and all have LREE depleted patterns (Figure 2). The five samples from dredge OCE23-14 are all plagioclase harzburgites of which only three (14-2, 14-3, and 14-10) have petrographic evidence for melt impregnation and two of these lack spinel. The other two plagioclase peridotites from this dredge have no petrographic evidence for melt impregnation, one has low TiO_2 spinel (0.06 wt %) and one contains somewhat elevated TiO_2 spinel (0.22 wt %), but both have LREE depleted patterns. Sample ALV616-1-1 is a plagioclase lherzolite with petrographic evidence of melt infiltration (photo 5 in supporting information Table S1) and elevated TiO_2 spinels (0.28 wt %) although it has a depleted LREE pattern.

The Nd-isotopic compositions of the diopsides vary from $^{143}Nd/^{144}Nd = 0.513122$ to 0.513425 (Figure 4). The sample with the highest $^{143}Nd/^{144}Nd$ and lowest $^{87}Sr/^{86}Sr$ is a plagioclase peridotite (ALV616-1-1) and has depleted trace element chemistry.

The trace element concentrations and isotopic compositions of 27 Cayman Rise basalts are listed in the supporting information Table S2. They show only limited variations in trace element and isotopic compositions and have nearly flat subparallel REE patterns: $(La/Sm)_N = 0.61–0.91$, $(La/Yb)_N = 0.89–1.47$. Cayman basalts range in $^{87}Sr/^{86}Sr$ from 0.702450 to 0.703142 and in $^{143}Nd/^{144}Nd$ from 0.513065 to 0.503158.

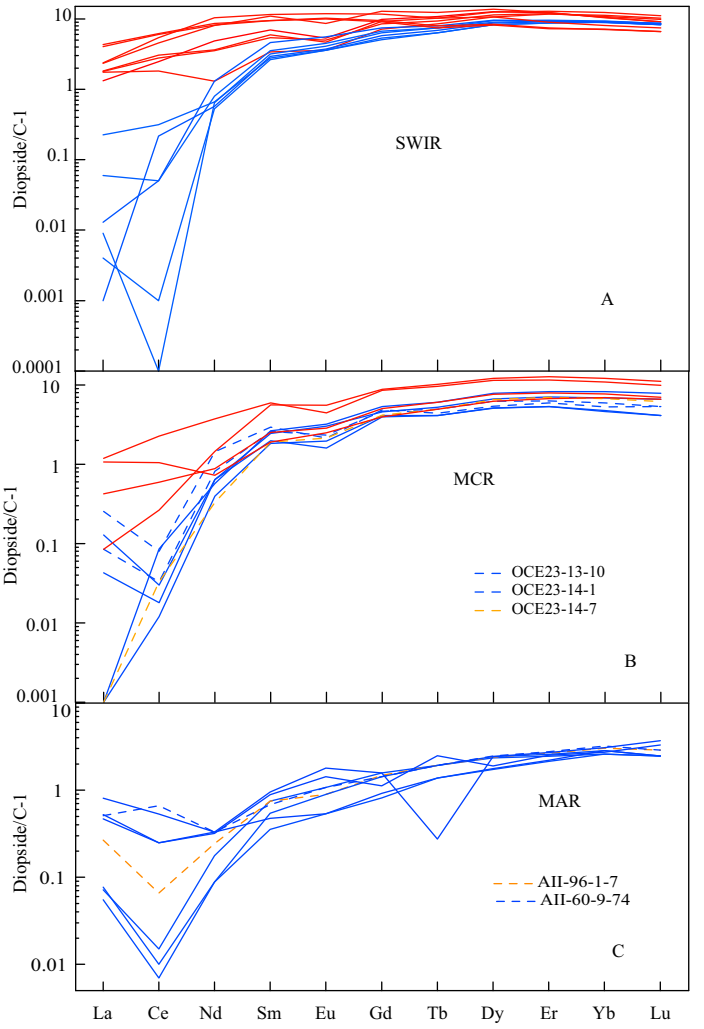

Figure 2. C-1 chondrite normalized [*McDonough and Sun*, 1995] REE patterns for diopsides in abyssal peridotites (a) of three dredges from Southwest Indian Ridge VAN7–78, VAN7–85, and VAN7–96. Blue patterns are for samples with less than 0.12 wt % TiO_2 in spinel, red patterns are for samples with spinels with >0.12 wt % TiO_2 in spinel that are impregnated with melt. (b) Mid-Cayman Rise; Blue patterns as in Figure 2a. Red patterns are impregnated peridotites. Hatched patterns are for residual plagioclase peridotites. Orange hatched pattern is a plagioclase peridotite with high TiO_2 spinel. (c) Mid-Atlantic Ridge samples. Patterns as in Figure 2b.

3.3. Mid-Atlantic Ridge (MAR)

Diopsides in our MAR peridotites (Table 1) display a restricted range in TiO_2 and Al_2O_3, but considerable scatter in Mg# and SiO_2 (diopside Mg# = 90–92, Al_2O_3 = 4.61–5.75 wt %) while spinel has a large range in Cr# (29–52) and $TiO_2 < 0.1\%$ with the exception of one spinel lherzolite (Figure 1). Diopside Na_2O and TiO_2 contents (0.09–0.38 wt % and 0.08–0.13 wt %, respectively) are at the depleted end of the peridotite spectrum (Figure 1).

Normalized REE patterns are plotted in Figure 2. The MAR peridotites are strongly depleted in light REE with Ce_N ranging from 0.007 to 0.66 and $(Ce/Yb)_N$ ranging from 0.002 to 0.20. Compared to SWIR and MCR, MAR peridotites have lower abundances of middle and heavy REE: $Dy_N \sim 2.15$, $Lu_N \sim 2.77$. The MAR peridotites have Nd-isotopic compositions ($^{143}Nd/^{144}Nd$ = 0.513011–0.513190) that are indistinguishable from the associated ridge basalts (Figure 4).

4. Discussion

4.1. Melt-Rock Relations Based on Major and Trace Elements

Interpretation of the chemical variations requires assessment as to what degree melts have interacted with residual peridotite during its recent ascent in the mantle; any reaction between melt and matrix does not necessarily progress to establishment of a new equilibrium. Interaction between melt and peridotite beneath mid-ocean ridges can be of many types but fall into two general categories: (1) reaction with dispersed melt which can be extreme in composition migrating through a near-fractionally melting mantle matrix, and (2) reaction and equilibration with MORB-like melt aggregated in a zone of focused transport representing different melting increments that themselves reflect variations in source mineralogy and chemistry.

Melt impregnation can be recognized chemically by increased TiO_2 in the spinel and increase in LREE in the diopside. Melt impregnation can also effect the major element chemistry of the diopside [*Dick et al*., 2010], however these chemical variations are less reliable indicators as the different types of melt impregnation have different effects[*Dick*, 1977; *Dick et al*., 1984; *Dick*, 1989; *Dijkstra et al*., 2001; *Kelemen and Dick*, 1995; *Liang*, 2003; *Quick*, 1981; *Seyler and Bonatti*, 1997].

We have the following criteria for a sample to be considered residual: (1) spinel with less than 0.12 wt % TiO_2, (2) a LREE depleted pattern for diopside, and (3) lack of petrographic evidence for melt infiltration. The limit on the TiO_2 content of the spinel is stricter than most other studies. Based on experimental data

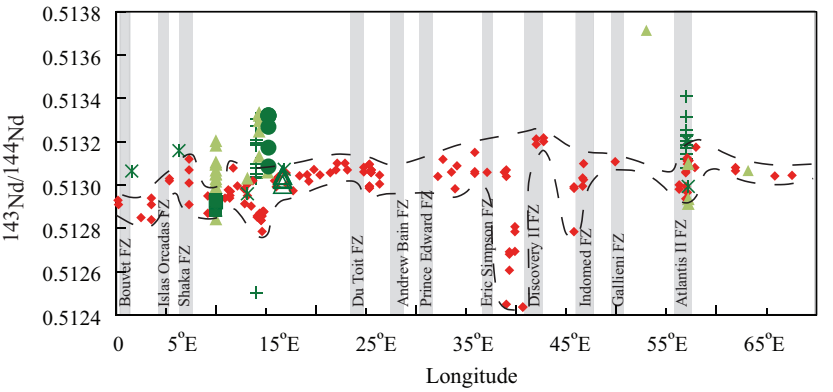

Figure 3. Nd-isotopic compositions of diopsides (green) peridotites and basalts (red) from SWIR—squares VAN7–96, circles VAN7–85, triangles VAN7–78, solid symbols—spinel peridotites and open symbols—plagioclase peridotites. Figure is an updated version of the figure published in *Salters and Dick* [2002]. Peridotites and basalt Nd-isotopic compositions are plotted against longitude. Other peridotite data from *Salters and Dick* [2002] (plusses); *Snow et al.* [1994] (stars), *Warren et al.* [2009] (triangles), and *Cipriani et al.* [2009] (triangles). Basalts data (diamonds) from: *le Roex et al.* [1983, 1989], *Mahoney et al.* [1992], and *Standish et al.* [2008].

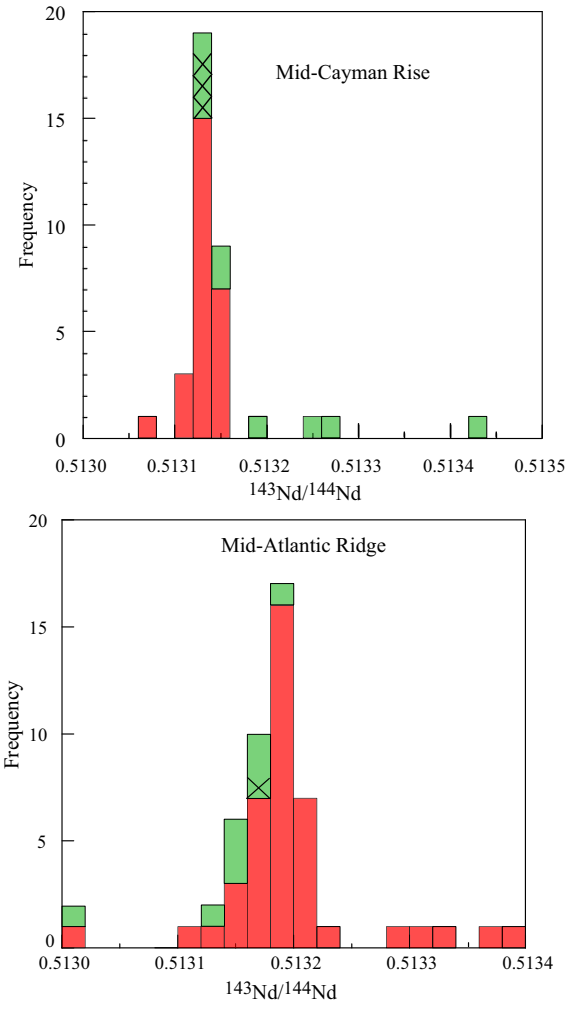

Figure 4. Histogram comparing the variation in Nd-isotopic composition of the peridotites with the associated basalts: (a) MCR, and (b) MAR. Peridotites that are considered impregnated with melt are indicated with a cross mark. Basalts data source from this study, *Donnelly et al.* [2004], *Ito et al.* [1987], and *Salters* [1996]. Green symbols are peridotites, red symbols are basalts.

[*Kinzler and Grove*, 1992; *Kinzler*, 1997; *Robinson et al.*, 1998] spinel D_{Ti} is between 0.15 and 0.2, and spinel with 0.12 wt % TiO_2 is in equilibrium with a melt with 0.6–0.8 wt % TiO_2. There are four peridotites that do not meet the TiO_2 criteria, but do meet the other two; they will be discussed separately. All other peridotites are considered to be either impregnated by melt or have reacted with melt. It should be noted that we found the absence or presence of plagioclase (or its pseudomorphs) is not as reliable indicator of melt impregnation as compared to the three criteria mentioned above.

Among the SWIR dredges, peridotites from two dredges have high Na_2O and TiO_2 diopside and high-TiO_2 spinel consistent with melt impregnation (Figure 1 and Table 1), while Dredge VAN7–85 peridotites meet all the residual criteria (see also Figure 2a). Using the measured concentrations and 1.2 GPa partition coefficients from *Salters and Longhi* [2002] melts in equilibrium with VAN7–96 diopsides are very similar to MORB-type melts. The VAN7–85 diopsides, however, have too low LREE and MREE to be in equilibrium with "local" MORB, indicating a dominantly residual origin consistent with their major element compositions and petrographic characteristics.

At the MCR, we have petrographically identified seven plagioclase-peridotites. Two of these peridotites (OCE23-13-10 and OCE23-14-1) as well as all spinel peridotites meet the three criteria for being considered residual. Of the remaining plagioclase peridotites four show petrographic evidence for melt infiltration (see also photo 5 in

supporting information Table S1) as well as major element characteristics consistent with melt impregnation: diopsides have high average Na_2O, SiO_2, and TiO_2 and lower Al_2O_3 (see Figure 1). These "impregnated" plagioclase peridotites also have higher Ce/Sm ratios than the "residual" peridotites, but similar HREE (see Figure 2b), indicating the chromatographic effect of a migrating exotic melt [*Navon and Stolper*, 1987].

The petrography of OCE23-14-7 is consistent with a residual character though it has relatively high TiO_2 spinel. However, its diopside REE pattern is strongly depleted (see Figure 2b). The partition coefficient of Ce and Nd in diopside is lower than partition coefficient of Ti in spinel ($D_{Ti} \sim 0.15$), and based on Cr and Al diffusion in spinel [*Suzuki et al*., 2008] the diffusion coefficient for Ti in spinel and Ce and Nd in diopside [*Van Orman et al*., 2001] are expected to be similar. Therefore, Ce and Nd contents in diopside are expected to be as sensitive if not more sensitive to melt impregnation as Ti in spinel, especially if this is an aggregated melt. The lack of LREE enrichment is thus strong evidence against melt impregnation. The plagioclase of OCE23-14-7, then, likely exsolved from aluminous pyroxene during decompression and emplacement. Plagioclase peridotite ALV616-1-1 has the most radiogenic Nd-isotopic composition ($\varepsilon_{Nd} = 15.51$). If this isotopic composition is influenced by impregnation this melt either needs to have a significant amount of TiO_2 to affect the spinel and either be REE depleted or have radiogenic Nd; i.e., an exotic melt.

Except for one plagioclase peridotite (AII-96-1-7), spinel TiO_2 contents of all MAR peridotites are low (Figure 1). The diopsides from MARK peridotites have lower HREE abundances than most other abyssal peridotites and they are too depleted to be in equilibrium with MORB. Four of the seven residual peridotites, however, have relatively high Ce/Yb and Ce/Sm. This has been explained by *Seyler et al*. [2011] as a reaction between a residual peridotite and a melt derived from the garnet stability field. Such a melt would be strongly LREE enriched but HREE depleted, and the resulting impregnated peridotite should have a LREE-enriched pattern and HREE-depletion compared to residual peridotites. The present pattern of low absolute abundance coupled with LREE depletion, the absence of textural or mineral-chemical evidence for melt infiltration, and the low TiO_2 content of the spinels indicates a history of depletion followed by an enrichment event and subsequent second depletion. Evidence for such ancient enrichment processes have also been found in the Gakkel Ridge peridotites when the REE were combined with Nd and Hf isotopes [*Stracke et al*., 2011].

In the final analysis, there are four out of the 36 peridotites that have an ambivalent character in that the TiO_2 content of the spinel is high, but other major and trace element chemistry as well as petrography is residual. In all other peridotites, the chemical and petrographic properties all are consistent with either a residual or impregnated character.

4.2. Trace Element Depletion and Enrichment Trends

It is argued that trace element variations like Ti versus Zr and Ce versus Yb are also important indicators of melt impregnation [*Brunelli et al*., 2006; *Hellebrand et al*., 2002]. These studies used a combination of major and trace elements, as well as textural evidence, to assess the degree to which peridotites are affected by melt infiltration either during or after melting. Elevated Zr and Ce contents for given Ti or Yb contents are sensitive indicators of melt impregnation. We examine to what degree this can be applied to our data using a depletion and refertilization model (Figure 5). The straight lines in Figure 5 are simple melt-depletion trends with Bulk Silicate Earth (blue) [*Brunelli et al*., 2006] or MORB source (black) [*Salters and Stracke*, 2004] as a starting composition. Samples that are significantly to the right of these lines are impregnated and depleted compared to the starting composition. Melt impregnation of peridotites with either an aggregated melt or a fractional melt quickly results in a deviation from simple melt-depletion trends and results in higher Zr for given Ti. If correct then a significant number of abyssal peridotites (small gray symbols) have seen melt infiltration. The residual peridotites from the SWIR and MCR fall on the depletion trend while some of the residual peridotites from MAR fall below the Bulk Silicate Earth depletion trend but along the MORB source depletion trend. However, melting trends are semiparallel in this diagram and depend on the details of the melting process and source. Table S3 in the supporting information reports our melt modes and partition coefficients, which are derived from experiments designed to investigate melting beneath mid-ocean ridge [*Longhi*, 2002; *Salters and Longhi*, 1999; *Salters et al*., 2002] and our best estimates of the depletion trend. Complex histories like depletion followed by enrichment, followed by depletion will also deviate from the single depletion trend. The curved lines are compositions that result from a depletion followed by refertilization. It can now be seen that the deviation from the blue depletion line could also be

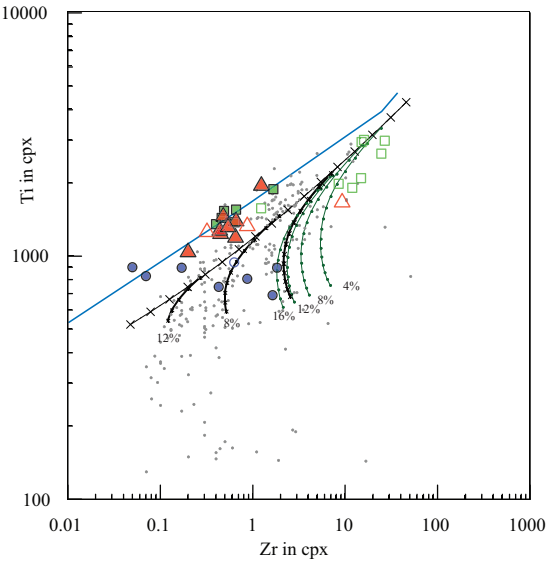

Figure 5. Abyssal peridotite diopside Ti and Zr (ppm). Scenario 1 represented by the black straight line is the depletion trend based on our melting model for diopside in the spinel peridotite field from a depleted peridotite source, with 1% melt-depletion increments. Blue line is a similar depletion trend based on the model of *Brunelli et al.* [2006], which assumes a bulk silicate earth source composition. Curved lines are the depletion trend of scenario 1 which is subsequently refertilized with 0.5% of melt. Different curves are for different melt compositions added. Green curves represent 0.5% addition of an aggregate melt of 4%, 8%, 12%, or 16% melting (labeled on curves) of a MORB source. Black curved lines represent 0.5% melt addition of a melt composition derived from a MORB source that has undergone 4%, 8%, or 12% fractional melting. Smaller gray symbols are abyssal peridotites from the same studies referenced in Figure 4.

related to source composition and a more complex history of depletion followed by enrichment and depletion.

We argue that Ti versus Zr variations are indeed sensitive to melt impregnation, however, whether this melt impregnation took place before or after a melting event cannot be discerned from these variations alone. Indeed *Stracke et al.* [2011] showed that some of the trace element and Hf-Nd isotope systematics are best modeled as due to ancient melt enrichment unrelated to recent melting.

4.3. Peridotite-Basalt Relationship

The basalts derived from the peridotites now reside some 10's of kilometers off axis, and thus a direct comparison of melt and residue is not possible. We assume that the spatial variation in the present-day basalts is similar to the temporal variation. This is supported by the along-axis correlation between spatially associated MORB and peridotite compositions found by *Dick et al.* [1984], where the basalts were essentially zero age while the peridotites ranged from 0.1 to 12 Ma in age. Furthermore, there is a length scale to MORB isotope variations [*Agranier et al.*, 2005; *Hanan et al.*, 2013; *Zindler and Hart*, 1986] indicating coherence in composition on several length scales. Thus, regional comparisons are probably more appropriate than global comparisons, although even on a global scale, the average $^{143}Nd/^{144}Nd$ ratio of abyssal peridotites is higher that of MORB.

Salters and Dick [2002] showed that at two SWIR locations the Nd-isotopic compositions of the abyssal peridotites and basalts are distinctly different. At mantle upwelling rates on the order of 10 mm/yr the post-melting radiogenic in-growth of the Nd-isotope affects the $^{143}Nd/^{144}Nd$ ratio at most at the tens of ppm level [$\ll$ 50 ppm ; see also *Stracke et al.*, 2011; *Warren et al.*, 2009]. We thus consider that radiogenic in-growth after melting did not significantly affect the Nd-isotopic composition of the peridotites. Peridotites from the VAN7–78 and VAN7–96 have Nd-isotopic compositions that lie within the range of the associated basalts. This observation fits with the petrographic (see supporting information Table S1) and chemical evidence of melt impregnation for VAN7–78 and VAN7–96 samples. The melt impregnation would have reset their isotopic compositions.

Basalts and peridotites at SWIR are statistically different even if the impregnated ones are included. *T* test of the Nd-isotopic composition of all available data, 67 basalts [*le Roex et al.*, 1983, 1989; *Mahoney et al.*, 1992; *Snow et al.*, 1994; *Standish*, 2006] and 69 peridotites from SWIR [*Cipriani et al.*, 2011; *Salters and Dick*, 2002; *Snow et al.*, 1994; *Warren et al.*, 2009; this study], show with a *t* probability of $<$0.001 that the peridotites and basalts are two distinct populations. The mean difference between basalt and peridotite in $^{143}Nd/^{144}Nd$ is 0.000141, while the standard deviation of $^{143}Nd/^{144}Nd$ is 0.000173 and 0.000086, respectively, for the peridotites and basalts. Thus, peridotites show a more variable Nd-isotopic composition than the basalts and there is significant overlap in composition. The mean difference between basalt and peridotite becomes larger when the impregnated peridotites are excluded for the statistical analysis.

At the Mid-Cayman-Rise, basalts display a narrow range in $^{143}Nd/^{144}Nd$. Twenty-nine basalts vary only from 0.513101 to 0.513190, and have relatively uniform trace element compositions (see Table 2). The range of Nd-isotopic compositions of peridotites from the MCR is larger (0.513122–0.513425) with more radiogenic

values than the basalts (Figure 4). The peridotites with more radiogenic compositions than the basalts are all "residual" peridotites and evidence for late-stage melt infiltration is absent. Except for ALV616-1-1 the "impregnated" peridotites all have isotopic compositions similar to the basalts. The radiogenic isotopic composition of ALV616-1-1 indicates that melts that are not fully aggregated MORB can be present in the peridotite. At the MCR the *t* probability of 0.04 shows that 15 basalts and 10 peridotites are also two distinct populations, even though we include the impregnated peridotites in this analysis. The mean difference between MCR basalt and peridotite in $^{143}Nd/^{144}Nd$ is 0.000060 while the standard deviation of $^{143}Nd/^{144}Nd$ is 0.000096 and 0.000009, respectively, for the peridotites and basalts.

MARK peridotite isotopic compositions are largely within the basalt range, with one sample having less radiogenic Nd than the basalts. The nearest MORB with an isotopic composition similar to the low $^{143}Nd/^{144}Nd$ peridotite is more than 600 km to the north, and it is clearly an outlier at MARK.

Stracke et al. [2011], *Stracke and Snow* [2009], and *Salters and Dick* [2011] together analyzed 39 peridotites form the Gakkel Ridge for Nd-isotopic composition. Compared to the Nd-isotopic composition of 47 Gakkel basalts [*Goldstein et al*., 2008] the average Gakkel peridotite is more radiogenic by 2.3 ε_{Nd}-units. *T* test shows a *t* probability of 0.008 that the Gakkel peridotites and basalts are distinct populations. The more radiogenic nature of the peridotite at the MCR (this study), the SWIR [*Cipriani et al*., 2011; *Warren et al*., 2009; this study], and Gakkel Ridge [*Salters and Dick*, 2011; *Stracke and Snow*, 2009; *Stracke et al*., 2011] indicates that the basalts are biased to a less depleted source. This is observed at N-MORB dominated ridge segments as well as those where an enriched component is more prominent in the basalt suites as at the SWIR between 9°E and 16°E [*le Roex et al*., 1992; *Standish et al*., 2008].

A disproportionate contribution of a less-depleted mantle component to the basalts can explain the difference with the peridotites. This can occur if the less-depleted component has a lower solidus temperature than the depleted component(s). The occurrence of a multisolidus mantle at ridge segments with N-MORB and segments with N and E-MORB indicates that its occurrence can be a ubiquitous feature of the subridge mantle, unrelated to a specific enriched composition. *Salters et al*. [2011] also argued for the presence of materials with different solidi in the MORB source based on the global Hf-Nd isotope systematics in MORB.

At MAR ridge segments adjacent to the Kane Fracture Zone the basalts have similar isotopic characteristics to the peridotites. Their REE patterns indicate that they cannot be simple residues of melting and that these peridotites have seen an impregnation event, followed by additional melting.

4.4. Nd-Model Ages for the Peridotites

The isotopic heterogeneity observed in residual peridotites is related to initial variations in the mantle composition that existed prior to the recent ridge-melting event. *Dick et al*. [1984], *Hellebrand et al*. [2001], and *Cipriani et al*. [2009] show that the average degree of peridotite depletion is correlated with the chemistry of spatially associated basalts, which is interpreted as a reflection of the degree of mantle melting. We can use this average degree of depletion then to calculate the hypothetical composition of the peridotites before the recent melting that formed the present-day ridge basalts, i.e., return the melt to the peridotite. The parent-daughter ratio of these hypothetical sources is then used to calculate model ages. This hypothetical model age, provided the assumptions are correct, is when the peridotite growth curve theoretically deviated from the bulk silicate Earth growth curve, and is the age of formation of that piece of depleted mantle. Noting that the assumptions are unlikely to all be correct, it is still worthwhile considering what these ages might tell us.

The degree of melting is estimated from the average REE patterns of the ridge basalts assuming a depleted mantle starting composition [*Salters and Stracke*, 2004]. This implies that the observed heterogeneities reflect differences in composition prior to recent melting. The estimated average degree of melting is between 4% and 6% for the SWIR and MCR, and we have used 4% for the calculations. For the MARK area the peridotite history is clearly more complicated than our scenario and the peridotites prior to the recent melting are clearly not average depleted mantle, and thus we exclude this location. We now approximate the Sm/Nd ratios of the individual peridotites before melting. This Sm/Nd ratio combined with the measured $^{143}Nd/^{144}Nd$, allows calculation of evolution lines for the individual peridotites prior to melting. The intercept between the peridotite evolution line and the bulk silicate earth (BSE) evolution line is taken as the model age for the peridotite. The model ages range from 2.4 Ga to future ages. Twenty percent of the

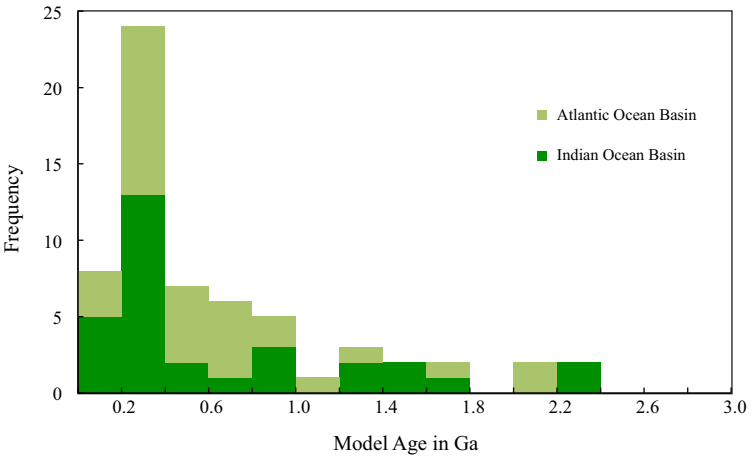

Figure 6. Histogram of Sm-Nd model ages for peridotites from this study and published peridotites [*Cipriani et al*., 2004; *Salters and Dick*, 2002; *Stracke et al*., 2011; *Warren et al*., 2009]. We calculated Sm/Nd ratios of peridotites before melting based on degree of melt estimates from the basalts. From the calculated Sm/Nd ratios and measured $^{143}Nd/^{144}Nd$ we calculated the time when peridotites deviated from the BSE evolution line, which is the model age for that peridotite.

peridotites yield unrealistic ages, either older than the age of the Earth (4%) or future ages (14%). These ages carry a significant uncertainty as the degree of melting is not known accurately, and the variation resulting from differences of recent melting among the individual samples is not well known. We have also made these age calculations for other published peridotite data primarily from the Vema Fracture Zone [*Cipriani et al*., 2004], additional SWIR data [*Salters and Dick*, 2002; *Warren et al*., 2009], and Gakkel Ridge [*Stracke et al*., 2011]. All realistic model ages are displayed in the histogram in Figure 6; the complete distribution of ages is in Table S4 of the supporting information. The important aspect of the model ages is that the age distribution is strongly skewed toward younger ages ($<$1 Ga).

As the readers have undoubtedly followed all of the reasoning in this paper with some care, they will realize that the assumptions made in the calculation of the model ages cannot be correct. In the first place, the very radiogenic $^{143}Nd/^{144}Nd$ ratios of many abyssal peridotites mean that the basalts oversample the low-melting $^{143}Nd/^{144}Nd$ mantle component. Thus, the actual theoretical model ages for the melting events shown in Figure 6 are biased toward older ages. Moreover, the mantle source compositions are not constant, and are now believed to vary significantly both along and between ridges. This is the result of complex cycles of mantle melting and refertilization that have undoubtedly repeated themselves in various ways over Earth history. The range of residual peridotite isotopic compositions as well as trace element compositions (see also Figure 5) requires a range of initial source compositions to explain, varying from that of bulk silicate Earth to compositions more depleted than the one given for our model. Thus, the present composition of any residual peridotite is the sum of all the prior melt events that have occurred to it over Earth history. Thus, our model ages are not only biased ages, but also are better interpreted as "average" ages that reflect these various events.

The Nd-model ages, however, agree with the Re-depletion ages of abyssal peridotites [*Brandon et al*., 2000; *Harvey et al*., 2006; *Liu et al*., 2008]. The Nd-model ages are interpreted to mark the maximum average time since deviation from a bulk Earth evolution. The average age of either the Nd-model ages or the Re-depletion ages is significantly younger than the 1.7 Ga indicated by the lead isotopes [*Zindler and Hart*, 1986] indicating this line has no direct age significance [*Rudge et al*., 2005; *Rudge*, 2006]. The older model ages suggest that some of the peridotites can retain the geochemical signature of an ancient melting history, although they were in convecting upper mantle for a long period of time. But the number of these peridotites is few and the majority cluster toward relatively young model ages. The young ages further suggest that our estimates of the depleted mantle composition based on one-stage, two-stage, or "continuous depletion" [*Salters and Stracke*, 2004; *Workman and Hart*, 2005] should be considered evolution paths averaging over a much larger variety of compositions at any given time. These ages are consistent with studies that explain the isotopic variations in MORB by multiple depletion events and relatively short turn-over time of the asthenosphere [*Albarede*, 2001; *Kellogg et al*., 2007; *Rudge et al*., 2005; *Rudge*, 2006].

5. Conclusions

At the SWIR and MCR, the mineralogical and chemical characteristics of the peridotites indicate that a subset was impregnated by melts. However, a significant number of the SWIR and MCR peridotites, as well as all MAR peridotites, record a residual signature.

The Nd-isotopic compositions of these "impregnated" peridotites are within the range of the spatially associated basalts, confirming they were produced by impregnation of the shallow mantle by aggregated MORB-like melts.

At the SWIR and MCR, Nd-isotopic compositions of the residual peridotites only partly overlap with Nd-isotopic compositions of the associated ridge basalts and extend toward more radiogenic ratios. This discrepancy in Nd-isotope ratios between abyssal peridotites and the associated ridge basalts can be explained by an underrepresentation of the sources' depleted component. At MAR the peridotites overlap in isotopic composition with the basalts, although the peridotites are characterized as residual. It is significant to note that the MCR is far away from any hot spot influence and the presence of a low-solidus component here indicates this component can be ubiquitous in the asthenosphere.

Calculated Nd-model ages suggest that the MORB mantle has a range of depletion ages that is skewed toward younger ages, less than 1 Ga. The oldest depletion is calculated to be as old as 2.4 Ga. This implies that much of the mantle has been processed relatively recently.

Acknowledgments

M. Bizimis is thanked for his help with the analyses as well as has function as a soundboard for the interpretation of the data. We also express our gratitude to Margaret Sulanowska for her assistance in sampling and curation. Numerous conversations with Eric Hellebrand, Stan Hart, and Jon Snow also contributed to our understanding of abyssal peridotite isotope and major element chemistry. We very much appreciate the lengthy, but thoughtful comments of Andreas Stracke, Danielle Brunelli, several anonymous reviewers and the reviews by John Rudge and Charles Langmuir. The research was supported by NSF grants OCE 0241053 and OCE 0930429 to Salters and OCE 0827825 to Dick.

References

Agranier, A., J. Blichert-Toft, D. Graham, V. Debaille, P. Schiano, and F. Albarede (2005), The spectra of isotopic heterogeneities along the mid-Atlantic Ridge, *Earth Planet. Sci. Lett.*, *238*, 96–109.

Albarede, F. (2001), Radiogenic ingrowth in systems with multiple reservoirs: Applications to the differentation of the mantle-crust system, *Earth Planet. Sci. Lett.*, *189*, 59–73.

Brandon, A. D., J. E. Snow, R. J. Walker, J. W. Morgan, and T. D. Mock (2000), ^{190}Pt-^{186}Os and ^{187}Re-^{187}Os systematics in abyssal peridotites, *Earth Planet. Sci. Lett.*, *177*, 319–335.

Brunelli, D., M. Seyler, A. Cipriani, L. Ottolini, and E. Bonatti (2006), Discontinuous melt extraction and weak refertilization of mantle peridotites at the Vema lithospheric section (Mid-Atlantic Ridge), *J. Petrol.*, *47*, 745–771.

Bryan, W. B., G. Thompson, and J. N. Ludden (1981), Compositional variation in normal MORB from 22°–25°N: Mid-Atlantic Ridge and Kane Fracture Zone, *J. Geophys. Res.*, *86*, 11,815–11,836.

Cipriani, A., H. Brueckner, E. Bonatti, and D. Brunelli (2004), Oceanic crust generated by elusive parents: Sr and Nd isotopes in basalt-peridotite pairs from the Mid-Atlantic Ridge, *Geology*, *32*(8), 657–660.

Cipriani, A., E. Bonatti, D. Brunelli, and M. Ligi (2009), 26 million years of mantle upwelling below a segment of the Mid Atlantic Ridge: The Vema Lithospheric Section revisited, *Earth Planet. Sci. Lett.*, *285*, 87–95.

Cipriani, A., E. Bonatti, and R. W. Carlson (2011), Nonchondritic ^{142}Nd in suboceanic mantle peridotite, *Geochem. Geophys. Geosyst.*, *12*, Q03006, doi:10.1029/2010GC003415.

Dick, H. J. B. (1977), Partial melting in Josephine peridotite. 1: Effect on mineral composition and its consequence for geobarometry and geothermometry, *Am. J. Sci.*, *277*(7), 801–832.

Dick, H. J. B. (1989), Abyssal peridotites, very slow spreading ridges and ocean ridge magmatism, in *Magmatism in the Ocean Basins*, edited by A. D. Saunders and M. J. Norry, pp. 71–105, Geol. Soc., London.

Dick, H. J. B., and T. D. Bullen (1984), Chromian spinel as a petrogenetic indicator in abyssal and alpine-type peridotite and spatially associated lavas, *Contrib. Mineral. Petrol.*, *86*(1), 54–76.

Dick, H. J. B., R. L. Fisher, and W. B. Bryan (1984), Mineralogical variability of the uppermost mantle along mid-ocean ridges, *Earth Planet. Sci. Lett.*, *69*, 88–106.

Dick, H. J. B., J. Lin, and H. Schouten (2003), An ultraslow-spreading class of ocean ridge, *Nature*, *426*, 405–412.

Dick, H. J. B., M. A. Tivey, and B. E. Tucholke (2008), Plutonic foundation of a slow spreading ridge segment: Oceanic core complex at Kane Megamullion, 23°30′N, 45°20′W, *Geochem. Geophys. Geosyst.*, *9*, Q05014, doi:10.1029/2007GC001645.

Dick, H. J. B., C. J. Lissenberg, and J. M. Warren (2010), Mantle melting, melt transport, and delivery beneath a slow-spreading ridge: The paleo-MAR from 23°15′N to 23°45′N, *J. Petrol.*, *51*(1–2), 425–467.

Dijkstra, A. H., M. R. Drury, and R. L. M. Vissers (2001), Structural petrology of plagioclase peridotites in the west Othris Mountains (Greece): Melt impregnation in the mantle lithosphere, *J. Petrol.*, *42*(1), 5–24.

Donnelly, K., S. J. Goldstein, C. H. Langmuir, and M. Spiegelman (2004), Origin of enriched ocean ridge basalts and implications for mantle dynamics, *Earth Planet. Sci. Lett.*, *226*, 347–366.

Elthon, D. (1992), Chemical trends in abyssal peridotites: Refertilization of depleted suboceanic mantle, *J. Geophys. Res.*, *97*, 9015–9025.

Georgen, J. E., and J. Lin (2003), Plume-transform interactions at ultra-slow spreading rates: Implications for the Southwest Indian Ridge, *Geochem. Geophys. Geosyst.*, *4*(9), 9106, doi:10.1029/2003GC000542.

Goldstein, S. J., G. Soffer, C. Langmuir, K. Lehnert, D. Graham, and P. J. Michael (2008), Origin of a 'Southern Hemisphere' geochemical signature in the Arctic upper mantle, *Nature*, *453*, 89–93.

Grindlay, N. R., P. J. Fox, and K. C. MacDonald (1991), Second-order ridge axis discontinuities in the south Atlantic: Morphology, structure and evolution, *Mar. Geophys. Res.*, *13*, 21–49.

Hanan, B. B., J. Blichert-Toft, C. Hemond, K. Sayit, A. Agranier, D. W. Graham, and F. Albarède (2013), Pb and Hf isotope variations along the Southeast Indian Ridge and the dynamic distribution of MORB source domains in the upper mantle, *Earth Planet. Sci. Lett.*, *375*, 196–208.

Harvey, J., A. Gannoun, K. W. Burton, N. W. Rogers, O. Alard, and I. J. Parkinson (2006), Ancient melt extraction from the oceanic upper mantle revealed by Re-Os isotopes in abyssal peridoties from the Mid-Atlantic Ridge, *Earth Planet. Sci. Lett.*, *244*(3–4), 606–621.

Hellebrand, E., J. E. Snow, H. J. B. Dick, and A. W. Hofmann (2001), Coupled major and trace elements as indicators of the extent of melting in mid-ocean-ridge peridotites, *Nature*, *410*, 677–681.

Hellebrand, E., J. E. Snow, P. Hoppe, and A. W. Hofman (2002), Garnet-field melting and Late-stage refertilization in 'Residual' abyssal peridotites from the Central Indian Ridge, *J. Petrol.*, *43*(12), 2305–2338.

Ito, E., W. M. White, and C. Goepel (1987), The O, Sr, Nd and Pb isotope geochemistry of MORB, *Chem. Geol.*, *62*, 157–176.

Johnson, K. T. M., H. J. B. Dick, and N. Shimizu (1990), Melting in the oceanic upper mantle: An ion microprobe study of diopsides in abyssal peridotites, *J. Geophys. Res.*, *95*, 2661–2678.
Kelemen, P. B., and H. J. B. Dick (1995), Focused melt flow and localized deformation in the upper mantle: Juxtaposition of replacive dunite and ductile shear zones in the Josephine peridotite, SW Oregon, *J. Geophys. Res.*, *100*, 423–438.
Kellogg, J. B., S. B. Jaconsen, and R. J. O'Connell (2007), Modeling lead isotopic heterogeneity in mid-ocean ridge basalts, *Earth Planet. Sci. Lett.*, *262*, 328–342.
Kinzler, R. J. (1997), Melting of mantle peridotite at pressures approaching the spinel to garnet transition, *J. Geophys. Res.*, *102*, 865–874.
Kinzler, R. J., and T. L. Grove (1992), Primary magmas of mid-ocean ridge basalts. Part 1: Experiments and methods, *J. Geophys. Res.*, *97*, 6885–6906.
Klein, E. M., and C. H. Langmuir (1987), Global correlations of ocean ridge basalt chemistry with axial depth and crustal thickness, *J. Geophys. Res.*, *92*, 8089–8115.
le Roex, A. P., H. J. B. Dick, A. J. Erlank, A. M. Reid, F. A. Frey, and S. R. Hart (1983), Geochemistry, mineralogy and petrogenesis of lavas erupted along the southwest Indian Ridge between the Bouvet Triple Junction and 11 degrees east, *J. Petrol.*, *24*, 267–318.
le Roex, A. P., H. J. B. Dick, and R. L. Fisher (1989), Petrology and geochemistry of MORB from 25°E to 46°E along the southwest Indian ridge: Evidence for contrasting styles of mantle enrichment, *J. Petrol.*, *30*, 947–986.
le Roex, A. P., H. J. B. Dick, and R. T. Watkins (1992), Petrogenesis of anomalous K-enriched MORB from the Southwest Indian Ridge: 11°53′E to 14°38′E, *Contrib. Mineral. Petrol.*, *110*, 253–268.
Liang, Y. (2003), Kinetics of crystal-melt reaction in partially molten silicates. 1: Grain scale processes, *Geochem. Geophys. Geosyst.*, *4*(5), 1045, doi:10.1029/2002GC000375.
Liu, C.-Z., J. E. Snow, E. Hellebrand, G. Brugmann, A. vonder Handt, A. Buchi, and A. W. Hofmann (2008), Ancient, highly heterogeneous mantle beneath Gakkel Ridge, Arctic Ocean, *Nature*, *452*, 311–315.
Longhi, J. (2002), Some phase equilibria systematics of lherzolite melting. I, *Geochem. Geophys. Geosyst.*, *3*(3), 1020, doi:10.1029/2001GC000204.
Macdonald, K. C., and T. L. Holcombe (1978), Inversion of magnetic-anomalies and sea-floor spreading in Cayman trough, *Earth Planet. Sci. Lett.*, *40*, 407–414.
Mahoney, J., A. P. Le Roex, Z. Peng, R. L. Fisher, and J. H. Natland (1992), Southwestern limits of Indian Ocean Ridge mantle and the origin of low $^{206}Pb/^{204}Pb$ mid-ocean ridge basalt: Isotope systematicsof the Central Southwest Indian Ridge (17°–50°E), *J. Geophys. Res.*, *97*, 19,771–19,790.
Mahoney, J. J., J. H. Natland, W. M. White, R. Poreda, S. H. Bloomer, R. L. Fisher, and A. N. Baxter (1989), Isotopic and geochemical provinces of the western Indian Ocean spreading centers, *J. Geophys. Res.*, *94*, 4033–4052.
Meyzen, C. M., J. N. Ludden, E. Humler, B. Luais, M. J. Toplis, C. Mevel, and M. Storey (2005), New insights into the origin and distribution of the DUPAL isotope anomaly in the Indian Ocean mantle from MORB of the Southwest Indian Ridge, *Geochem. Geophys. Geosyst.*, *6*, Q11K11, doi:10.1029/2005GC000979.
Meyzen, C. M., J. Blichert-Toft, J. N. Ludden, E. Humler, C. Mevel, and F. Albarede (2007), Isotopic portrayal of the Earth's upper mantle flow field, *Nature*, *447*, 1069–1074.
Michael, P. J., and E. Bonatti (1985), Peridotite composition from the North Atlantic: Regional and tectonic variations and implications for partial melting, *Earth Planet. Sci. Lett.*, *73*, 91–104.
Montesi, L. G. J., and M. D. Behn (2007), Mantle low and melting underneath oblique and ultraslow mid-ocean ridges, *Geophys. Res. Lett.*, *34*, L23407, doi:10.1029/2007GL031067.
Navon, O., and E. Stolper (1987), Geochemical consequences of melt percolation: The upper mantle as a chromatographic column, *J. Geol.*, *95*, 285–307.
Perfit, M. R. (1976), Petrology and geochemistry of mafic rocks from the Cayman Trench: Evidence for spreading, *Geology*, *5*, 105–110.
Perfit, M. R., and B. C. Heezen (1978), Geology and evolution of Cayman trench, *Geol. Soc. Am. Bull.*, *89*, 1155–1174.
Quick, J. E. (1981), The origin and significance of large, tabular dunite bodies in the trinity peridotite, northern California, *Contrib. Mineral. Petrol.*, *78*, 413–422.
Reynolds, J. R., and C. H. Langmuir (1997), Petrological systematics of the mid-Atlantic ridge south of Kane: Implications for ocean crust formation, *J. Geophys. Res.*, *102*, 14,915–14,946.
Robinson, J. A. C., B. J. Wood, and J. D. Blundy (1998), The beginning of melting of fertile and depleted peridotite at 1.5 GPa, *Earth Planet. Sci. Lett.*, *155*, 97–111.
Rudge, J. F. (2006), Mantle pseudo-isochrons revisited, *Earth Planet. Sci. Lett.*, *249*(3–4), 494–513.
Rudge, J. F., D. McKenzie, and P. H. Haynes (2005), A theretical approach to understanding the isotopic heterogeneity of mid-ocean ridge basalt, *Geochim. Cosmochim. Acta*, *69*(15), 3873–3887.
Salters, V. J. M. (1996), The generation of mid-ocean ridge basalts from the Hf and Nd isotope perspective, *Earth Planet. Sci. Lett.*, *141*, 109–123.
Salters, V. J. M., and H. J. B. Dick (2002), Mineralogy of the mid-ocean ridge basalt source from neodymium isotopic composition in abyssal peridotites, *Nature*, *418*, 68–72.
Salters, V. J. M., and H. J. B. Dick (2011), Ultra depleted mantle at the Gakkel Ridge based on Hafnium and Neodymium isotopes, *Eos Trans. AGU*, *92*(52), Fall Meeting Suppl., Absract V41G-02.
Salters, V. J. M., and J. E. Longhi (1999), Trace element partitioning during the initial stages of melting beneath ocean ridges, *Earth Planet. Sci. Lett.*, *166*, 15–30.
Salters, V. J. M., and A. Stracke (2004), The composition of the depleted mantle, *Geochem. Geophys. Geosyst. 5*, Q05B07, doi:10.1029/2003GC000597.
Salters, V. J. M., J. Longhi, and M. Bizimis (2002), Near mantle solidus trace element partitioning at pressures up to 3.4 GPa, *Geochem. Geophys. Geosyst.*, *3*(7), 1038, doi:10.1029/2001GC000148.
Salters, V. J. M., S. Mallick, S. R. Hart, C. H. Langmuir, and A. Stracke (2011), Domains of depleted mantle: New evidence from hafnium and neodymium isotopes, *Geochem. Geophys. Geosyst.*, *12*, Q08001, doi:10.1029/2011GC003617.
Seyler, M., and E. Bonatti (1997), Regional-scale melt-induced remelting of lherzolitic mantle in the Romanche Fracture Zone (Atlantic Ocean), *Earth Planet. Sci. Lett.*, *146*, 273–287.
Seyler, M., D. Brunelli, M. J. Toplis, and M. Cannat (2011), Multiscale chemical heterogeneities beneath the eastern Southwest Indian Ridge (52°E–68°E): Trace element compositions of along axis dredged peridotites, *Geochem. Geophys. Geosyst.*, *12*, Q0AC15, doi:10.1029/2011GC003585.

Snow, J. E., S. R. Hart, and H. J. B. Dick (1994), Nd and Sr isotope evidence linking mid-ocean ridge basalts and abyssal peridotites, *Nature*, *371*, 57–60.
Standish, J. J. (2006), The influence of ridge geometry at the ultraslow-spreading Southwest Indian Ridge (9°–25°E): Basalt composition sensitivity to variations in source and process, PhD thesis, 286 pp., Mass. Inst. of Technol. and Wood Hole Oceanogr. Inst., Woods Hole.
Standish, J. J., H. J. B. Dick, P. J. Michael, W. G. Melson, and T. O'Hearn (2008), MORB generation beneath the ultraslow spreading Southwest Indian Ridge (9–25°E): Major element chemistry and the importance of process versus source, *Geochem. Geophys. Geosyst.*, *9*, Q05004, doi:10.1029/2008GC001959.
Stracke, A., and J. E. Snow (2009), The Earth's mantle is more depleted than we thought, *Eos Trans. AGU*, *90*(52), Fall Meeting Suppl., Abstract V24A-03.
Stracke, A., J. E. Snow, E. Hellebrand, A. von der Handt, B. Bourdon, K. Birbaum, and D. Günther (2011), Abyssal peridotite Hf isotopes identify extreme mantle depletion *Earth Planet. Sci. Lett.*, *308*(3–4), 359–368.
Suzuki, A. M., A. Yasuda, and K. Ozawa (2008), Cr and Al diffusion in chromite spinel: Experimental determination and its implication for diffusion creep, *Phys. Chem. Miner.*, *35*, 433–445.
Thompson, G., W. B. Bryan, and W. G. Melson (1980), Geological and geophysical investigation of the Mid-cayman Rise spreading center: Geochemical variation and petrogenesis of basalt glasses, *J. Geol.*, *88*, 41–55.
Van Orman, J., T. Grove, and N. Shimizu (2001), Rare earth element diffusion in diopside: Influence in temperature, pressure, and ionic radius, and an elastic model for diffusion in silicates, *Contrib. Mineral. Petrol.*, *141*, 687–703.
Warren, J. M., N. Shimizu, C. Sakaguchi, H. J. B. Dick, and E. Nakamura (2009), An assessment of upper mantle heterogeneity based on abyssal peridotite isotopic compositions, *J. Geophys. Res.*, *114*, B12203, doi:10.1029/2008JB006186.
Wendt, J. I., M. Regelous, Y. Niu, R. Hékinian, and K. D. Collerson (1999), Geochemistry of lavas from the Garrett Transform Fault: Insights into mantle heterogeneity beneath the eastern Pacific, *Earth Planet. Sci. Lett.*, *173*, 271–284.
White, R. S., T. A. Minshull, M. J. Bickle, and C. J. Robinson (2001), Melt generation at very slow-spreading oceanic ridges: Constraints from geochemical and geophysical data, *J. Petrol.*, *42*, 1171–1196.
Workman, R. K., and S. R. Hart (2005), Major and trace element composition of the depleted MORB mantle (DMM), *Earth Planet. Sci. Lett.*, *231*(1–2), 53–72.
Zhou, H., and H. J. B. Dick (2013), Thin crust as evidence for depleted mantle supporting the Marion Rise, *Nature*, *494*(7436), 195–200.
Zindler, A., and S. R. Hart (1986), Chemical geodynamics, *Ann. Rev. Earth Planet. Sci.*, *14*, 493–571.

Erratum

In the originally published version of this article, the first two samples VAN-7-78-36H and VAN-78-36V were missing from Table 2. The table has since been corrected and this version may be considered the authoritative version of record.